

NANO EXPRESS

Open Access



Enhanced Photocatalytic Hydrogen Evolution by Loading $\text{Cd}_{0.5}\text{Zn}_{0.5}\text{S}$ QDs onto Ni_2P Porous Nanosheets

Lingfeng Xiao¹, Tong Su¹, Zhuo Wang^{2*}, Kun Zhang³, Xiaoni Peng¹, Yibo Han³, Quan Li⁴ and Xina Wang^{1*} 

Abstract

Ni_2P has been decorated on CdS nanowires or nanorods for efficient photocatalytic H_2 production, whereas the specific surface area remains limited because of the large size. Here, the composites of $\text{Cd}_{0.5}\text{Zn}_{0.5}\text{S}$ quantum dots (QDs) on thin Ni_2P porous nanosheets with high specific surface area were constructed for noble metal-free photocatalytic H_2 generation. The porous Ni_2P nanosheets, which were formed by the interconnection of 15–30 nm-sized Ni_2P nanoparticles, allowed the uniform loading of 7 nm-sized $\text{Cd}_{0.5}\text{Zn}_{0.5}\text{S}$ QDs and the loading density being controllable. By tuning the content of Ni_2P , H_2 generation rates of $43.3 \mu\text{M h}^{-1}$ (1 mg photocatalyst) and $700 \mu\text{M h}^{-1}$ (100 mg photocatalyst) and a solar to hydrogen efficiency of 1.5% were achieved for the $\text{Ni}_2\text{P}-\text{Cd}_{0.5}\text{Zn}_{0.5}\text{S}$ composites. The effect of Ni_2P content on the light absorption, photoluminescence, and electrochemical property of the composite was systematically studied. Together with the band structure calculation based on density functional theory, the promotion of Ni_2P in charge transfer and HER activity together with the shading effect on light absorption were revealed. Such a strategy can be applied to other photocatalysts toward efficient solar hydrogen generation.

Keywords: Ni_2P , $\text{Cd}_{0.5}\text{Zn}_{0.5}\text{S}$, Nanosheet, Quantum dot, Hydrogen evolution

Background

As an efficient strategy to produce H_2 by utilizing solar energy, photocatalytic hydrogen production has attracted extensive attention since TiO_2 was reported as a photocatalyst in 1972 [1]. Compared with TiO_2 , $\text{Cd}_x\text{Zn}_{1-x}\text{S}$ shows excellent visible-light driven catalytic activity because of the narrower band gap and good photochemical stability. A H_2 production rate as high as $1097 \mu\text{M h}^{-1} \text{g}^{-1}$ has been achieved by using $\text{Cd}_{0.5}\text{Zn}_{0.5}\text{S}$ as photocatalyst [2], which composition has been proven to be the optimum for photocatalytic property. To decrease carrier recombination and prompt carrier separation for hydrogen evolution reaction (HER), noble metals such as Pt, Co-Pt, Ru, Au, and Pd have been used as co-catalysts [3–8]. For example, when co-catalyzed with Co-

Pt, the photocatalytic H_2 generation rate of $\text{Cd}_{0.5}\text{Zn}_{0.5}\text{S}$ quantum dots (QDs) could be increased by 4.7-folds [4]. A H_2 production as high as $\sim 6.3 \text{ mM h}^{-1} \text{mg}^{-1}$ was achieved when CdZnS was combined with Au [9]. However, the high cost of noble-metals greatly limits the future application in large scale, which makes the non-precious co-catalysts to be good candidates of precious ones for photocatalytic H_2 generation.

Among the various non-noble co-catalysts including carbon family (graphene, carbon nanotubes, reduced graphene oxide, carbon nanodots) [10–15], phosphides [16–22], and TiO_2 [23, 24] and sulfides [25–32], Ni_2P and CoP have been extensively composited with CdS nanowires and/or nanorods for efficient photocatalytic H_2 production [16–18, 33–36]. In these composites, one-dimensional (1D) CdS was always decorated by smaller phosphides' nanoparticles or nanosheets with HER activity, and carrier recombinations can be greatly reduced because of the long carrier diffusion length of the 1D structure and its well-defined hetero-interface with the co-catalysts. Considering the advantages of QDs such as its high solar energy to fuel conversion

* Correspondence: wangzh@hubei.edu.cn; xnwang2006@hotmail.com

²State Center for Designer Low-Carbon and Environmental Materials, Zhengzhou University, 100 Kexue Avenue, Zhengzhou 450001, China

¹Hubei Collaborative Innovation Center for Advanced Organic Chemical Materials, Hubei Key Laboratory of Ferro & Piezoelectric Materials and Devices, Faculty of Physics and Electronic Science, Hubei University, Wuhan 430062, China

Full list of author information is available at the end of the article

efficiency, low fabrication costs [37, 38], and HER mainly occurs at co-catalyst/electrolyte interface, it is rational to construct hetero-nanostructures with plenty of specific surface area of active sites while still maintaining fast carrier separation. In this case, a reverse structure with photocatalysts loaded onto co-catalysts was reported for efficient photocatalytic H_2 generation [10, 13]. For instance, hydrogen generation rates of 2.08 and $\sim 33.4 \text{ mM h}^{-1} \text{ mg}^{-1}$ were established by loading $\text{Cd}_{0.5}\text{Zn}_{0.5}\text{S}$ QDs onto onion-like carbon and 2D graphitic carbon nitride (g- C_3N_4) microribbons, respectively. These make it highly expectable for photocatalytic H_2 generation if phosphide nanostructures were decorated by $\text{Cd}_{0.5}\text{Zn}_{0.5}\text{S}$ QDs. However, such a reverse structure has been rarely reported up to now.

Here, a reverse structure of $\text{Cd}_{0.5}\text{Zn}_{0.5}\text{S}$ QDs on Ni_2P nanosheet arrays was synthesized by thermal solution method for enhanced photocatalytic H_2 generation. A hydrogen generation rate of $700 \mu\text{M h}^{-1}$ (with 100 mg feeding catalyst) and a solar to hydrogen efficiency (STH) of 1.5% were achieved at 1.5 wt% of Ni_2P . The effect of Ni_2P on the H_2 generation rate, optical, and electrochemical property of the composite was systematically studied. Moreover, the band structure of Ni_2P was calculated based on density functional theory, together with the photo-electrochemical property, the detailed role of Ni_2P for the H_2 generation was revealed.

Methods/experimental

Synthesis of Co-catalyst

Firstly, 20 mL deionized water containing 2.61 g nickel nitrate and 2.52 g hexamethylenetetramine was transferred to a Teflon autoclave and heated at 120°C for 10 h for the formation of NiOOH . After cooled down to room temperature, the NiOOH product was washed by alcohol and deionized water via centrifugation at 2000 rpm for three times and each time for 5 min. Then, a mixture of 0.22 g NiOOH and 0.44 g sodium hypophosphite was put into a tube furnace and heated at 500°C for 2 h for phosphorizing. When it naturally cooled down to room temperature, black Ni_2P powder was obtained and collected.

Synthesis of $\text{Ni}_2\text{P}-\text{Cd}_{0.5}\text{Zn}_{0.5}\text{S}$ Nanocomposites

To prepare $\text{Ni}_2\text{P}-\text{Cd}_{0.5}\text{Zn}_{0.5}\text{S}$ composite, 100 mg Ni_2P powder was dispersed into 20 mL ethanol via ultrasonic processing for 1 h. Then x mL ($x = 0.48, 0.96, 1.4, 3, 5$) well-dispersed Ni_2P solution was added into a 20 mL ethylene glycol solution containing 272.6 mg ZnCl_2 and 456.7 mg $\text{CdCl}_2 \cdot 2.5\text{H}_2\text{O}$, and was heated to 170°C with continuous stirring under nitrogen protection. After the addition of 20 mL ethylene glycol solution dissolving 960.7 mg $\text{Na}_2\text{S} \cdot 9\text{H}_2\text{O}$, the solution was heated to 180°C and held for 1 h for the growth of $\text{Cd}_{0.5}\text{Zn}_{0.5}\text{S}$ on Ni_2P .

Finally, the samples were washed by alcohol and deionized water respectively for three times. By weighing the final $x\text{Ni}_2\text{P}-\text{Cd}_{0.5}\text{Zn}_{0.5}\text{S}$ composites, the weight percents (wt%) were determined to be 0.5 ($x = 0.48$), 1 ($x = 0.96$), 1.5 ($x = 1.4$), 3 ($x = 3$), 5 ($x = 5$). As a comparison, pure $\text{Cd}_{0.5}\text{Zn}_{0.5}\text{S}$ QDs were synthesized via the similar method except the addition of Ni_2P .

Morphology, Structure, and Optical Properties

Characterization

The morphology, microstructure, and composition were characterized by field emission scanning electron microscopy (FESEM, JSM-7100F, JEOL) and transmission electron microscopy (TEM, FEI Tecnai 20) equipped with scanning transmission electron microscopy (STEM) and energy dispersive X-ray spectroscopy (EDX). Powder X-ray diffraction (XRD) patterns were recorded on a Bruker AXS D8 X-ray diffractometer with $\text{Cu K}\alpha$ ($\lambda = 1.54056 \text{ \AA}$). Elemental composition, chemical, and valence states were studied by (valence band) X-ray photoelectron spectroscopy (XPS) measurements (XPS, Escalab 250Xi) with $\text{Al K}\alpha$ radiation. UV-Vis absorption was investigated by an UV-Vis spectrophotometer (UV-3600, Shimadzu) equipped with an integrating sphere device, and the weight/volume ratio of sample to deionized water was kept at 1 mg/10 mL. Photoluminescence (PL) measurements were carried out on a 7000 FL spectrophotometer (Hitachi, F7000) with an excitation wavelength of 400 nm. Before the PL measurements, pure $\text{Cd}_{0.5}\text{Zn}_{0.5}\text{S}$ QDs and the composites were well dispersed in ethanol, and the concentration of $\text{Cd}_{0.5}\text{Zn}_{0.5}\text{S}$ was maintained at 0.5 mg/mL for all the samples.

Linear Sweep Voltammetry (LSV) and Electrochemical Impedance Spectra (EIS) Measurements

LSV measurements were conducted in 1 M NaOH electrolyte ($\text{pH} = 14$) in an electrochemical work station (CHI 760E, CH Instruments) with a typical three-electrode configuration. A Pt foil and a saturated Ag/AgCl were used as the counter and reference electrode, respectively. The potentials were converted to those vs reversible hydrogen electrode (RHE) by the equation $E(\text{vs RHE}) = E(\text{vs Ag}/\text{AgCl}) + E_{\text{Ag}/\text{AgCl}}(\text{ref}) + 0.0591 \text{ V} \times \text{pH}$, where $(E_{\text{Ag}/\text{AgCl}}(\text{ref}) = 0.1976 \text{ V vs NHE (normal hydrogen electrode) at } 25^\circ\text{C})$ [39]. Electrochemical impedance spectra (EIS) measurements were carried out in darkness at 0.5 V vs RHE with an amplitude of 5 mV and the electrolyte of 0.35 M Na_2SO_3 and 0.25 M Na_2S aqueous solution by using a similar three-electrode system. The working electrode was made via spreading ~ 2 mg product (dispersed in 5 mL ethanol) over 4 cm^2 area FTO substrate and dried at 70°C for 5 h. The frequency range was kept within 0.1 Hz \sim 100 kHz, and

the spectra were analyzed by the Z-View program (Scribner Associates Inc.).

Photocatalytic (PC) H₂ Generation

Before H₂ production, the photocatalysts with different mass (1, 5, and 10 mg) were dispersed in a sealed quartz reactor (volume 40 mL, 5 cm × 5 cm × 1.6 cm) with 15 mL 0.75 M Na₂S and 1.05 M Na₂SO₃ aqueous solution. After degassing for 30 min by nitrogen, the photocatalytic experiment was performed under the irradiation of a 300 W Xe (PLS-SXE300/300UV, Perfect Light) lamp with a cut-off filter of 420 nm and an incident power of 300 mW/cm². The catalytic solution was kept continually stirring during the whole PC experiment. In every hour, 1-mL gas production was collected and analyzed by a gas chromatograph (GC-2018, Shimadzu, Japan, TCD). Further cycling stability experiment was performed under the same condition. Paralleling experiments with the feeding dosage of photocatalysts from 15 to 100 mg were conducted in 100 mL electrolyte of

Na₂S and Na₂SO₃ in a larger reactor (volume 150 mL) under the same illumination. The solar to hydrogen efficiency (STH) was calculated by the flowing equation:

$$\text{STH (\%)} = \frac{\text{energy of generated H}_2}{\text{light energy onto the surface of solution}} \times 100\%$$

$$= \frac{237\text{KJ/mole} \times \text{moles of H}_2 \text{ produced}}{\text{area of solution been irradiated} \times 300\text{mW/cm}^2} \times 100\%$$

Computational Methods

The energy and electronic properties of bulk Ni₂P were calculated using density functional theory (DFT) method. Vienna Ab-initio Simulation Package (VASP) [40] was adopted during the calculations with the projector augmented wave pseudo potentials (PAW) [41], and the Perdew-Burke-Ernzerhof type (PBE) generalized gradient approximation (GGA) [42] exchange–correlational functional methods. A Brillouin zone with a 9 × 9 × 9 Monkhorst–Pack Γ point grid [43], a kinetic energy cut off with 450 eV, and an energy criterion of 10^{−6} eV were

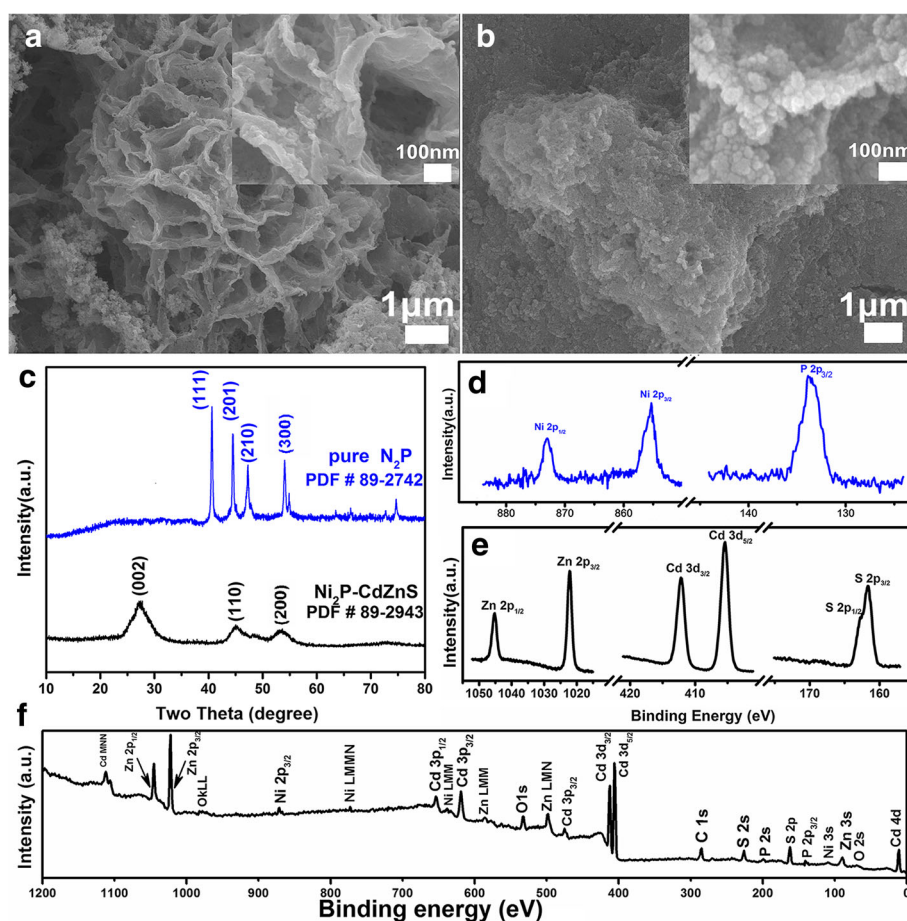


Fig. 1 Morphology, crystalline property, and chemical states of Ni₂P-Cd_{0.5}Zn_{0.5}S composites (1.5 wt% Ni₂P). **a–b** Low and high (inset) magnification SEM images of Ni₂P before and after the loading of Cd_{0.5}Zn_{0.5}S, **c** XRD pattern of Ni₂P and Ni₂P-Cd_{0.5}Zn_{0.5}S, **d–f** XPS fine and survey spectra of Ni₂P-Cd_{0.5}Zn_{0.5}S composite

applied for geometric optimization until the residual forces were converged to less than 0.01 eV/Å. The bulk model of hexagonal Ni_2P with P-62M symmetry was taken into account. After fully structure optimized, the lattice parameter of Ni_2P ($a = b = 5.86918$ Å, and $c = 3.37027$ Å) can be obtained, which is well consistent with the reported values [44].

Results and Discussion

Figure 1a, b show the morphology of Ni_2P before and after the composition with $\text{Cd}_{0.5}\text{Zn}_{0.5}\text{S}$ QDs (Ni_2P wt%: 1.5%). Pure Ni_2P has a flower-like morphology which is composed of many crossed nanosheets with the thickness less than 20 nm and planar size from several tens nanometer to micrometer scope. From the XRD pattern of pure Ni_2P in Fig. 1c, diffraction peaks of (111), (201), (210), and (300) planes can be clearly observed at 40.7° , 44.6° , 47.4° , and 54.2° , respectively, which correspond to hexagonal Ni_2P (JCPDF no. 89-2742). After loaded by $\text{Cd}_{0.5}\text{Zn}_{0.5}\text{S}$ QDs, the surface of the nanosheets become rather rough, and plenty of nanoparticles with size less than 10 nm can be distinguished on the pristine Ni_2P skeleton. At the same time, the XRD refraction peaks of $\text{Cd}_{0.5}\text{Zn}_{0.5}\text{S}$ (JCPDF no. 89-2943) (100), (002), (101), and (110) planes can be clearly found at 26.0° , 27.8° , 29.6° ,

and 45.9° , respectively [6, 45], while the diffraction signal of Ni_2P is greatly depressed because of the low weight ratio (1.5 wt%) of Ni_2P to $\text{Cd}_{0.5}\text{Zn}_{0.5}\text{S}$. The coexistence of $\text{Cd}_{0.5}\text{Zn}_{0.5}\text{S}$ and Ni_2P was demonstrated by the X-ray photoelectron spectrometer (XPS) fine and survey spectra in Fig. 1d–f. Except the oxygen and carbon signals arising from the air absorption, only Ni, P, Cd, Zn, and S can be detected, which rules out the possibility of other impurities. The peaks at 855.5 and 873.9 eV can be assigned to Ni $2p_{3/2}$ and $2p_{1/2}$, respectively, and the peak of P $2p_{3/2}$ can be found at 133.6 eV [16, 46]. Concurrently, the doublet peaks of Zn 2p, Cd 3d, and S 2p suggest the bivalent Zn^{2+} , Cd^{2+} , and S^{2-} from $\text{Cd}_{0.5}\text{Zn}_{0.5}\text{S}$ QDs [3, 34, 47]. In brief, the growth of $\text{Cd}_{0.5}\text{Zn}_{0.5}\text{S}$ on Ni_2P nanosheets has been established for the formation of $\text{Ni}_2\text{P}-\text{Cd}_{0.5}\text{Zn}_{0.5}\text{S}$ nanocomposites.

The microstructure and elemental composition of the samples were further investigated by TEM-related techniques. From the different magnification TEM images of pure Ni_2P (Fig. 2a, b), the nanosheets are porous and composed of cross-linked irregular nanoparticles with size of ~ 15 –30 nm. The selected area electron diffraction pattern (SAED) in Fig. 2c shows the diffraction ring of Ni_2P (111), (201), (210), and (300) planes. The diffractive signals of high-index planes such as (222), (402),

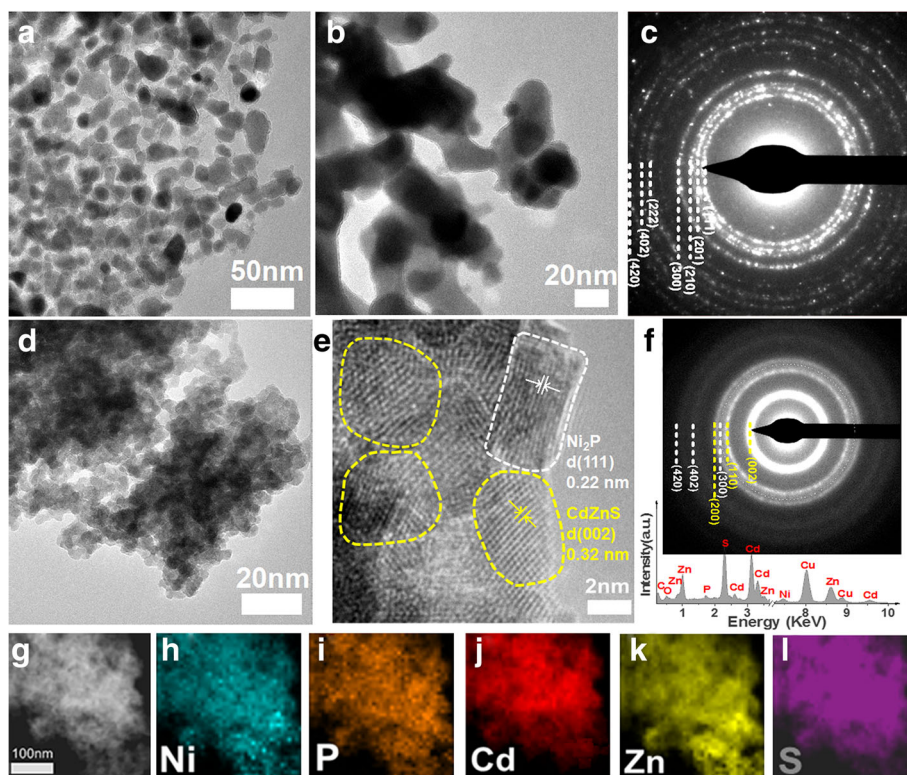


Fig. 2 Microstructure of Ni_2P and $\text{Ni}_2\text{P}-\text{Cd}_{0.5}\text{Zn}_{0.5}\text{S}$ composite. **a–c** and **d–f** Different-magnification TEM images and SAED pattern of Ni_2P and $\text{Ni}_2\text{P}-\text{Cd}_{0.5}\text{Zn}_{0.5}\text{S}$, the inset **f** is EDX spectrum, where the yellow and white dash lines denote $\text{Cd}_{0.5}\text{Zn}_{0.5}\text{S}$ and Ni_2P , respectively. **g** High-angle annular dark field (HAADF)-STEM image, and **h–l** the corresponding EDX mappings of $\text{Ni}_2\text{P}-\text{Cd}_{0.5}\text{Zn}_{0.5}\text{S}$ composite

and (420) can also be detected due to the strong multi-scattering of the high-energy electrons. After composited with $\text{Cd}_{0.5}\text{Zn}_{0.5}\text{S}$, the intercrossed Ni_2P nanosheets were covered by plenty of smaller nanoparticles with size of ~ 7 nm (Fig. 2d). The EDX spectra (inset, Fig. 2f) clearly shows the signal of Ni, P, Cd, Zn, and S, indicative of the coexistence of Ni_2P and $\text{Cd}_{0.5}\text{Zn}_{0.5}\text{S}$. From the SAED pattern (Fig. 2f), strong diffractive rings of $\text{Cd}_{0.5}\text{Zn}_{0.5}\text{S}$ (002), (110), and (200) planes (denoted by yellow dash lines) can be clearly distinguished along with the weak signals of Ni_2P (300), (402), and (420) (marked by white dash lines), suggesting the good composition of Ni_2P with QDs. It is noticeable that Ni_2P (300) ring overlaps with $\text{Cd}_{0.5}\text{Zn}_{0.5}\text{S}$ (110) and (200) planes, making it hard to be distinguished. The high-resolution TEM image of Ni_2P - $\text{Cd}_{0.5}\text{Zn}_{0.5}\text{S}$ sample in Fig. 2e further shows the lattice fringes with spacing of 0.34 and 0.22 nm, which corresponds to the $\text{Cd}_{0.5}\text{Zn}_{0.5}\text{S}$ (002) and Ni_2P (111) crystal planes, respectively. The elemental EDX mappings (Fig. 2h–l) taken from the region shown by the high-angle annular dark field (HAADF) image (Fig. 2g) exhibit that Ni, P, Cd, Zn, and S are distributed uniformly among the sample, further demonstrating the successful composition of $\text{Cd}_{0.5}\text{Zn}_{0.5}\text{S}$ QDs with the porous Ni_2P nanosheets.

Figure 3a shows the H_2 evolution rate of Ni_2P - $\text{Cd}_{0.5}\text{Zn}_{0.5}\text{S}$ nanocomposites varied with the content of Ni_2P at the feeding dosage of 1 mg in a 40 mL reactor. Pure $\text{Cd}_{0.5}\text{Zn}_{0.5}\text{S}$ shows a photocatalytic H_2 evolution rate of $12.6 \mu\text{M h}^{-1} \text{mg}^{-1}$, and pure Ni_2P shows negligible hydrogen generation. With the addition of Ni_2P , the photocatalytic activity of the Ni_2P - $\text{Cd}_{0.5}\text{Zn}_{0.5}\text{S}$ composites has been obviously enhanced and reaches the highest value of $43.3 \mu\text{M h}^{-1} \text{mg}^{-1}$ at 1.5 wt% Ni_2P , nearly 3.4 times higher than pure $\text{Cd}_{0.5}\text{Zn}_{0.5}\text{S}$. Further addition of Ni_2P (≥ 3 wt%) will result in fast degradation of property, and the H_2 evolution rate is less than pure $\text{Cd}_{0.5}\text{Zn}_{0.5}\text{S}$ when Ni_2P increases to 5 wt%. Such a non-linear behavior suggests that there exist an optimum Ni_2P content, namely, an appropriate loading density of $\text{Cd}_{0.5}\text{Zn}_{0.5}\text{S}$ on Ni_2P for the photocatalytic property. At the same time, the stability of 1.5 wt% Ni_2P - $\text{Cd}_{0.5}\text{Zn}_{0.5}\text{S}$ was studied by cycling test (Fig. 3b). During four successive cycles that lasted for totally 16 h, the H_2 generation maintained relative stable with negligible degradation, indicating the good photocatalytic stability of the composite.

The effect of the amount of catalyst on STH efficiency and H_2 generation was systematically studied (Fig. 3c–d)

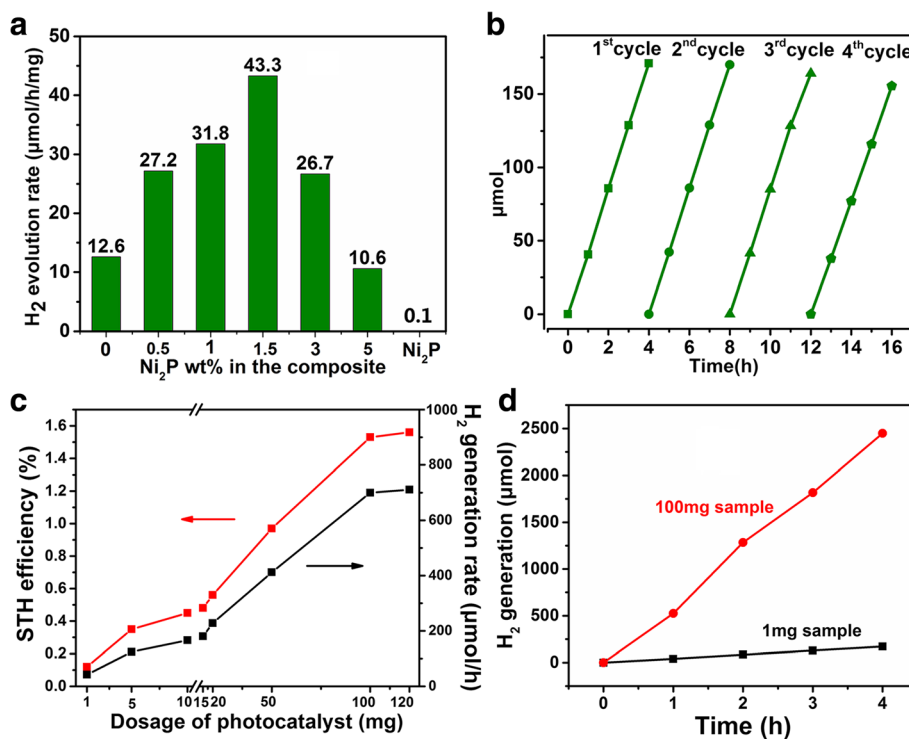


Fig. 3 Photocatalytic property of Ni_2P - $\text{Cd}_{0.5}\text{Zn}_{0.5}\text{S}$ composites. **a** Photocatalytic hydrogen generation at different wt% of Ni_2P and **b** the cycling test of the composite with 1.5 wt% of Ni_2P tested in a small reactor (40 mL, 1.0 mg photocatalyst). **c** Hydrogen production rate and solar to hydrogen efficiency (STH) at various amount of photocatalyst. The tests for the photocatalyst of dosage from 15 to 100 mg were carried out in a 150 mL reactor, and those of dosage from 1 to 10 mg were in a 40 mL reactor. **d** The hydrogen generation rate for 1 and 100 mg composite samples (1.5 wt% Ni_2P)

for 1.5 wt% $\text{Ni}_2\text{P}-\text{Cd}_{0.5}\text{Zn}_{0.5}\text{S}$ sample. Two typical reactors with volume of 40 and 150 mL were adopted at the same illumination power density. When tested in the smaller reactor (40 mL), though both the STH and H_2 generation rate increase with the catalyst's dosage from 1 to 10 mg, the increased step is far less than that of the dosage. The STH and H_2 generation rate are only 0.45% and $166 \mu\text{M h}^{-1}$ when the dosage of the catalyst increased to 10 mg, nearly 3.8 times of the 1 mg sample. For the larger reactor (150 mL), distinct increase in STH and H_2 generation can be found with the dosage increased from 15 to 100 mg, and a 1.53% STH and a $700 \mu\text{M h}^{-1}$ of H_2 generation can be achieved at the dosage of 100 mg, nearly 3.1 times of the 15 mg catalyst. Considering that the incident light has longer path when it passes through a deeper reactor, such a result shows that larger reactor will be more beneficial for the utilization of the incident light. However, the STH efficiency will be saturated once the dosage increased to about 100 mg, suggesting there exists an optimum dosage for the light utilization. The optimum H_2 generation rate is superior than $\text{CdZnS QDs-2D g-C}_3\text{N}_4$ microribbons (H_2 generation rate $33.4 \text{ mM h}^{-1} \text{ g}^{-1}$) [10], $\text{Cd}_{0.1}\text{Zn}_{0.9}\text{S}$ nanoparticles-carbon nanotubes (rate: $1563 \mu\text{M h}^{-1} \text{ g}^{-1}$) [11], a sandwich-structured $\text{C}_3\text{N}_4/\text{Au}/\text{CdZnS}$ photocatalyst (rate $6.15 \text{ mM h}^{-1} \text{ g}^{-1}$) [9], and $\text{CdS QDs-sensitized Zn}_{1-x}\text{Cd}_x\text{S}$ solid solutions (rate $2128 \mu\text{M h}^{-1} \text{ g}^{-1}$) [48].

To reveal the mechanism for the enhanced photocatalytic property and detailed role of Ni_2P , both the optical and electrochemical property of pure Ni_2P , $\text{Cd}_{0.5}\text{Zn}_{0.5}\text{S}$, and the composites were studied by Fig. 4. From the absorption spectra (Fig. 4a), pure $\text{Cd}_{0.5}\text{Zn}_{0.5}\text{S}$ exhibits an absorption edge at 506 nm, corresponding to the band gap of 2.45 eV [13, 49]. For pure Ni_2P (the inset), wide absorption over the whole visible range can be found. After the composition, besides the absorption in range $< 506 \text{ nm}$, obvious tails over the visible wavelength $> 506 \text{ nm}$ can be found, which can be attributed to the contribution from Ni_2P . As the visible absorption in longer wavelength increases with Ni_2P , the composite shows reduced absorption of $\text{Cd}_{0.5}\text{Zn}_{0.5}\text{S}$ ($< 506 \text{ nm}$). At the same time, the photoluminescence spectra (Fig. 4b) exhibit that pure $\text{Cd}_{0.5}\text{Zn}_{0.5}\text{S}$ has intensive band edge luminescence at $\sim 620 \text{ nm}$ when excited at the wavelength of 400 nm. After composition, it will be degraded gradually with the addition of Ni_2P . Considering that higher content of Ni_2P will induce more $\text{Ni}_2\text{P}/\text{Cd}_{0.5}\text{Zn}_{0.5}\text{S}$ interfaces which help to enhance charge transfer and suppress charge recombination, the decrease of PL intensity can be understood by the reduced carrier recombination and enhanced charge transfer at the $\text{Ni}_2\text{P}/\text{Cd}_{0.5}\text{Zn}_{0.5}\text{S}$ interface.

The effective role of Ni_2P in prompting charge transfer can also be reflected by the EIS spectra depending on Ni_2P content (Fig. 4c). As shown by the equivalent

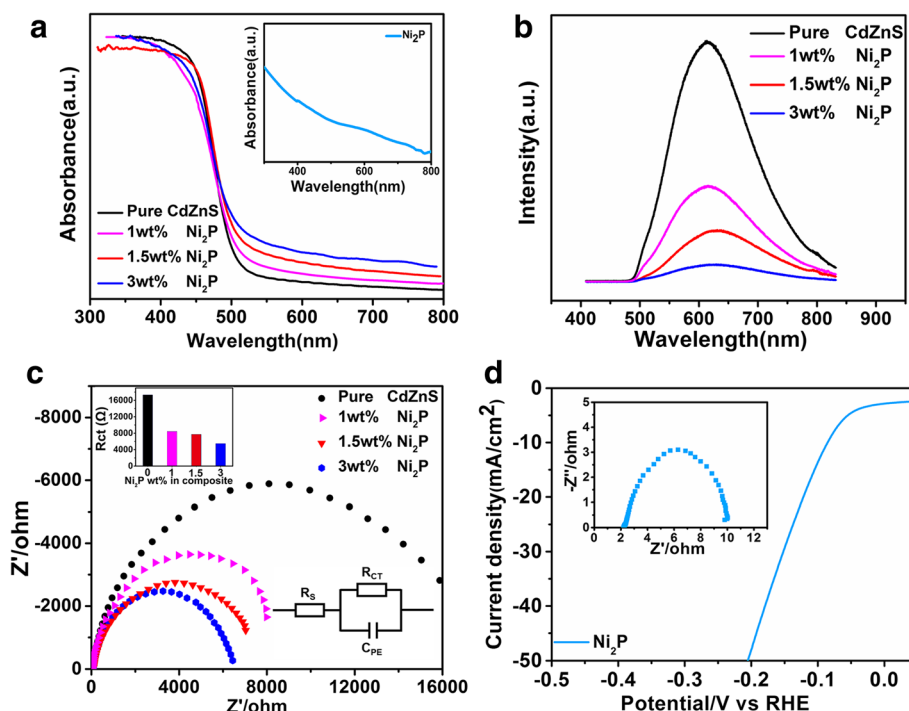


Fig. 4 The effect of Ni_2P content on the optical and electrochemical properties of $\text{Ni}_2\text{P}-\text{Cd}_{0.5}\text{Zn}_{0.5}\text{S}$ composite. **a** UV-Vis absorption spectra (inset pure Ni_2P), **b** photoluminescence spectra, and **c** EIS spectra. **d** LSV curve and EIS (inset) spectrum of pure Ni_2P

circuit (inset, Fig. 4c), the charge transfer resistance (R_{CT}) at catalyst/electrolyte interface can be evaluated by the semicircle radius of the Nyquist plots based on R-C equivalent circuit. The equivalent series resistance (ESR) can be obtained from the intersection of the curve and the real resistance (Z') axis, while the charge-transfer resistance (R_{CT}) corresponds to the width of the semicircle plotted at higher frequencies. The R_{CT} of pure $Cd_{0.5}Zn_{0.5}S$ is 17,320 Ω , indicative of its semiconductor nature. After the composition with 1, 1.5, and 3 wt% Ni_2P , R_{CT} decreases gradually to 8432, 7721, and 5473 Ω , respectively, suggesting the enhancement of Ni_2P in the electrical conductivity. Indeed, Ni_2P has been considered as a good electrocatalyst toward HER [44, 50, 51]. From the LSV curve of pure Ni_2P on Ni foam shown in Fig. 4d, the Ni_2P has good HER activity with overpotentials of 84 mV and 201 mV to attach the current density of 10 and 50 mA/cm^2 (without iR-correction), respectively. The EIS spectrum (inset Fig. 4d) exhibits that Ni_2P has a very low R_{CT} ($\sim 7.3 \Omega$), indicating the metallic character of Ni_2P . Therefore, Ni_2P can not only increase the electrical conductivity at $Cd_{0.5}Zn_{0.5}S/Ni_2P$ interface, but also supply effective active sites for HER, then leading to enhanced photocatalytic property of the composite.

Considering that the addition of Ni_2P decreased the absorption at wavelength < 506 nm, it is necessary to demonstrate whether the light absorption of Ni_2P can be utilized to generate hydrogen. The band structure of Ni_2P was then studied by DFT calculation. Figure 5a, b presents the ball and stick model of bulk Ni_2P and the calculated band structure. From Fig. 5b, no band gap can be detected, suggesting the metallic characteristic of Ni_2P , which agrees well with the above EIS result. This indicates that the photoelectrons are mainly attributed to the photo-excitation of $Cd_{0.5}Zn_{0.5}S$ rather than Ni_2P . Moreover, the Fermi level of Ni_2P (obtained from out car file) locates at 1.03 V vs. NHE, much lower than the conductive band minimum (CBM) level (-1.04 V vs NHE) of $Cd_{0.5}Zn_{0.5}S$ QDs [13].

Accordingly, the schematic mechanism was demonstrated for the photocatalytic H_2 evolution of the composite by Fig. 5c. The location of Fermi level of Ni_2P makes it energetically favorable for the transfer of photo-generated electrons from $Cd_{0.5}Zn_{0.5}S$ to Ni_2P , then prompts the separation of photo-excited electrons and holes at the interface, resulting in the depression of charge recombination. Concurrently, H_2 will evolve efficiently at the active sites of Ni_2P due to the good HER

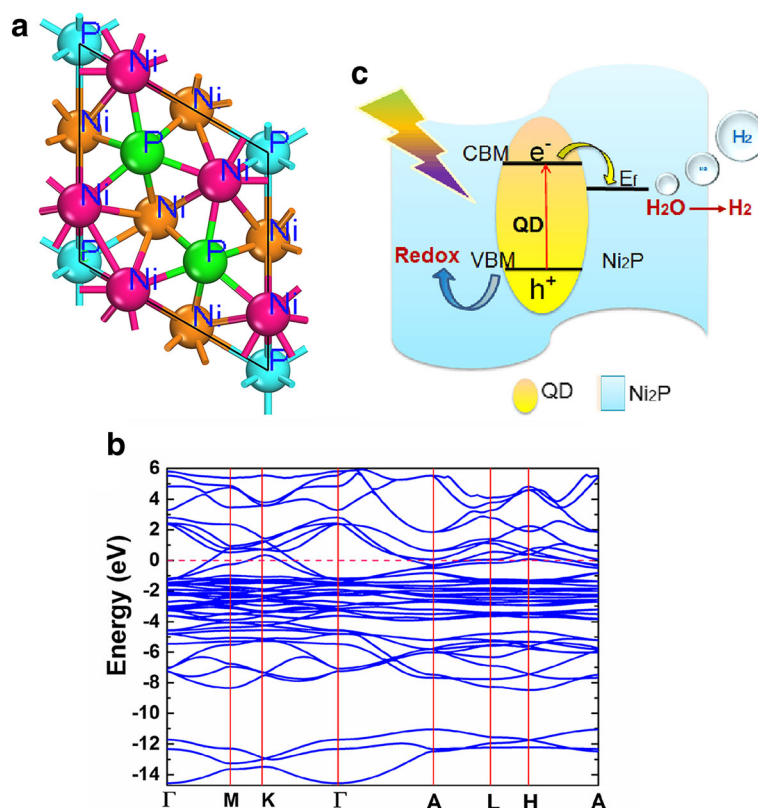


Fig. 5 The band diagram and charge separation and transfer mechanism for the photocatalytic H_2 evolution. **a** Top views of the ball and stick model of (001) surface-terminated bulk Ni_2P . **b** Calculated band structure of Ni_2P where the red dash line represents Fermi level. **c** Schematic mechanism illustrating the charge separation and transfer for the photocatalytic H_2 generation

activity and large specific surface area of the composites. The positive roles of Ni₂P in charge transfer and HER activity will dominate at the lower content of Ni₂P (≤ 1.5 wt%). When the content surpasses 1.5 wt%, the shading effect of Ni₂P in light absorption will overcome the positive aspect, leading to the degradation of H₂ generation. An optimum photocatalytic property will be achieved at 1.5 wt% Ni₂P when the two effects reach a balance.

Conclusions

A reverse structure of Cd_{0.5}Zn_{0.5}S QDs on Ni₂P porous nanosheets were fabricated for efficient photocatalytic H₂ production. The Ni₂P porous nanosheets were composed of 15–30-nm-sized nanoparticles that allows the effective loading of 7-nm-sized Cd_{0.5}Zn_{0.5}S QDs. As the charge separation and transfer property is enhanced with the addition of Ni₂P from 0 to 5 wt%, a competitive shading effect that unbeneficial for the light absorption of Cd_{0.5}Zn_{0.5}S is induced. An optimum photocatalytic H₂ generation of 43.3 $\mu\text{M h}^{-1}$ (dosage 1 mg) will be achieved at 1.5 wt% Ni₂P. Based on the optimum content, the photocatalytic dependence on feeding dosage of catalyst shows that the STH efficiency will reach the highest value of 1.5% at the dosage of 100 mg. The high HER activity and band structure of Ni₂P were revealed, confirming the effective role of Ni₂P in prompting photocatalytic H₂ evolution dynamics from both experimental and theoretical aspects. The heterostructure of Cd_{0.5}Zn_{0.5}S QDs-Ni₂P porous nanosheets can not only help to prompt the photo-excited charge separation and transfer, but also speed up the dynamics of hydrogen evolution reaction via the co-catalytic role of Ni₂P, thus enhances the photocatalytic hydrogen generation property. Such a method can be applied to other catalysts toward efficient photocatalytic property.

Abbreviations

CBM: Conductive band minimum; DFT: Density functional theory; EDX: Energy dispersive X-ray spectroscopy; EIS: Electrochemical impedance spectra; FESEM: Field emission scanning electron microscopy; FTO: Fluorine-doped tin oxide; GGA: Generalized gradient approximation; HER: Hydrogen evolution reaction; LSV: Linear sweep voltammetry; NHE: Normal hydrogen electrode; PBE: Perdew-Burke-Ernzerhof type; PC: Photocatalytic; PL: Photoluminescence; QDs: Quantum dots; RHE: Reversible hydrogen electrode; STEM: Scanning transmission electron microscopy; STH: Solar to hydrogen; TEM: Transmission electron microscopy; VASP: Vienna Ab-initio Simulation Package; XPS: X-ray photoelectron spectroscopy; XRD: X-ray diffraction

Acknowledgements

This work was supported by the National Natural Science Foundation of China (nos. 51472080, 51602094, 11104097), Open Research Fund Program of the State Key Laboratory of Low-dimensional Quantum Physics (no. KF201705), and Excellent Youth Foundation of Hubei Province (no. 2017CFA038). We thank the helps on DFT part from Prof. Zhongbin Huang and Dr. Hui Yang from Center for Computational Science, HUPPET.

Fundings

National Natural Science Foundation of China (51472080, 51602049, and 11104097) and Open Research Fund Program of the State Key Laboratory of Low-dimensional Quantum Physics.

Availability of Data and Materials

The datasets supporting the conclusions of this article are included within the article.

Authors' Contributions

XNW carried out the experimental design and the experimental data analysis. LFX prepared the Cd_{0.5}Zn_{0.5}S and Ni₂P-Cd_{0.5}Zn_{0.5}S samples and performed the XRD, SEM, XPS characterization and performed the LSV, EIS, PC, and stability tests. TS and ZW carried out the theoretical calculations. KZ, XNP, and YBH performed the PL measurements. QL performed the TEM characterization. All authors read and approved the final manuscript.

Competing Interests

The authors declare that they have no competing interests.

Publisher's Note

Springer Nature remains neutral with regard to jurisdictional claims in published maps and institutional affiliations.

Author details

¹Hubei Collaborative Innovation Center for Advanced Organic Chemical Materials, Hubei Key Laboratory of Ferro & Piezoelectric Materials and Devices, Faculty of Physics and Electronic Science, Hubei University, Wuhan 430062, China. ²State Center for Designer Low-Carbon and Environmental Materials, Zhengzhou University, 100 Kexue Avenue, Zhengzhou 450001, China. ³Wuhan National High Magnetic Field Center and School of Physics, Huazhong University of Science and Technology, Wuhan 430072, China. ⁴Department of Physics, The Chinese University of Hong Kong, Hong Kong, China.

Received: 29 November 2017 Accepted: 6 January 2018

Published online: 02 February 2018

References

1. Fujishima A, Honda K (1972) Electrochemical photolysis of water at a semiconductor electrode. *Nature* 238:37–38
2. Wang Y, Wu J, Zheng J, Xu R (2011) Highly active Zn_xCd_{1-x}S photocatalysts containing earth abundant elements only for H₂ production from water under visible light. *Catal Sci Technol* 1:940–947
3. Wang D-H, Wang L, Xu A-W (2012) Room-temperature synthesis of Zn_{0.80}Cd_{0.20}S solid solution with a high visible-light photocatalytic activity for hydrogen evolution. *Nano* 4:2046–2053
4. Wang H, Li Y, Shu D, Chen X, Liu X, Wang X, Jun Z, Wang H (2016) CoPt_x-loaded Zn_{0.5}Cd_{0.5}S nanocomposites for enhanced visible light photocatalytic H₂ production. *Int J Energ Res* 40:1280–1286
5. Navarro R, Del Valle F, Fierro J (2008) Photocatalytic hydrogen evolution from CdS-ZnO-CdO systems under visible light irradiation: effect of thermal treatment and presence of Pt and Ru cocatalysts. *Int J Hydrogen Energ* 33:4265–4273
6. Busby E, Thibert A, Page LE, Jawaid AM, Snee PT, Larsen DS (2013) Primary charge carrier dynamics of water-solubilized CdZnS/ZnS core/shell and CdZnS/ZnS-pd nanoparticle adducts. *Chem Phys Lett* 573:56–62
7. Gaikwad A, Tyagi D, Betty C, Sasikala R (2016) Photocatalytic and photo electrochemical properties of cadmium zinc sulfide solid solution in the presence of Pt and RuS₂ dual co-catalysts. *Appl Catal A-Gen* 517:91–99
8. Wang P, Sheng Y, Wang F, Yu H (2018) Synergistic effect of electron-transfer mediator and interfacial catalytic active-site for the enhanced H₂-evolution performance: a case study of CdS-au photocatalyst. *Appl Catal B-Environ* 220:561–569
9. Ma X, Jiang Q, Guo W, Zheng M, Xu W, Ma F, Hou B (2016) Fabrication of g-C₃N₄/Au/CdZnS Z-scheme photocatalyst to enhance photocatalysis performance. *RSC Adv* 6:28263–28269
10. Yao L, Wei D, Ni Y, Yan D, Hu C (2016) Surface localization of CdZnS quantum dots onto 2D g-C₃N₄ ultrathin microribbons: highly efficient visible light-induced H₂-generation. *Nano Energy* 26:248–256

11. Yu J, Yang B, Cheng B (2012) Noble-metal-free carbon nanotube- $\text{Cd}_{0.1}\text{Zn}_{0.9}\text{S}$ composites for high visible-light photocatalytic H_2 -production performance. *Nano* 4:2670–2677
12. Ibrahim S, Chakraborty K, Pal T, Ghosh S (2017, 1832) Solution processable RGO-CdZnS composite for solar light responsive photocatalytic degradation of 4-Nitrophenol. *Aip Conf Proc*:050005
13. Zhou X, Wang X, Feng X, Zhang K, Peng X, Wang H, Liu C, Han Y, Li Q (2017) Loading $\text{Cd}_{0.5}\text{Zn}_{0.5}\text{S}$ QDs onto onion-like carbon nanoparticles to boost photocatalytic hydrogen generation. *ACS Appl Mater Inter* 9:22560–22567
14. Xie G, Zhang K, Fang H, Guo B, Wang R, Yan H, Fang L, Gong JR (2013) A photoelectron chemical investigation on the synergetic effect between CdS and reduced graphene oxide for solar-energy conversion. *Chem-Asian J* 8: 2395–2400
15. Hu Y, Gao X, Yu L, Wang Y, Ning J, Xu S, Lou X (2013) Carbon-coated CdS petalous nanostructures with enhanced photostability and photocatalytic activity. *Angew Chem Int Edit* 125:5746–5749
16. Gao WZ, Xu Y, Chen Y, Fu WF (2015) Highly efficient and selective photocatalytic reduction of nitroarenes using the $\text{Ni}_2\text{P}/\text{CdS}$ catalyst under visible-light irradiation. *Chem Commun* 51:13217–13220
17. Zhao D, Sun B, Li X, Qin L, Kang S, Wang D (2016) Promoting visible light-driven hydrogen evolution over CdS nanorods using earth-abundant CoP as a cocatalyst. *RSC Adv* 6:33120–33125
18. Cao S, Chen Y, Wang CJ, He P, Fu WF (2014) Highly efficient photocatalytic hydrogen evolution by nickel phosphide nanoparticles from aqueous solution. *Chem Commun* 50:10427–10429
19. Cao S, Chen Y, Wang CJ, Lv XJ, Fu WF (2015) Spectacular photocatalytic hydrogen evolution using metal-phosphide/CdS hybrid catalysts under sunlight irradiation. *Chem Commun* 51:8708–8711
20. Cao S, Chen Y, Hou CC, Lv XJ, Fu WF (2015) Cobalt phosphide as a highly active non-precious metal cocatalyst for photocatalytic hydrogen production under visible light irradiation. *J Mater Chem A* 3:6096–6101
21. Wen J, Xie J, Shen R, Li X, Luo X, Zhang H, Zhang A, Bi G (2017) Markedly enhanced visible-light photocatalytic H_2 generation over $\text{g-C}_3\text{N}_4$ nanosheets decorated by robust nickel phosphide (Ni_3P_2) cocatalysts. *Dalton* 46:1794–1802
22. Liu S, Han L, Liu H. (2016) Synthesis, characterization and photocatalytic performance of $\text{PbS}/\text{Ni}_3\text{P}$ flowers. *App Surf Sci* 387:393–398
23. Li Y, Wang L, Liang J, Gao F, Yin K, Dai P (2017) Hierarchical Heterostructure of ZnO/TiO_2 hollow spheres for highly efficient photocatalytic hydrogen evolution. *Nanoscale Res Lett* 12(1):531
24. Tang H, Chang S, Jiang L, Tang G, Liang W (2016) Novel spindle-shaped nanoporous TiO_2 coupled graphitic $\text{g-C}_3\text{N}_4$ nanosheets with enhanced visible-light photocatalytic activity. *Ceram Int* 42:18443–18452
25. Zong X, Wu G, Yan H, Ma G, Shi J, Wen F, Wang L, Li C (2010) Photocatalytic H_2 evolution on MoS_2/CdS catalysts under visible light irradiation. *J Phys Chem C* 114:1963–1968
26. Cheng F, Xiang Q (2016) A solid-state approach to fabricate a CdS/CuS nano-heterojunction with promoted visible-light photocatalytic H_2 -evolution activity. *RSC Adv* 6:76269–76272
27. Yin X-L, Li L-L, Jiang W-J, Zhang Y, Zhang X, Wan L-J, Hu J-S (2016) MoS_2/CdS nanosheets-on-nanorod heterostructure for highly efficient photocatalytic H_2 generation under visible light irradiation. *ACS Appl Mater Inter* 8:15258–15266
28. Jen-La Plante I, Teitelboim A, Pinkas I, Oron D, Mokari T (2014) Exciton quenching due to copper diffusion limits the photocatalytic activity of $\text{CdS}/\text{Cu}_2\text{S}$ nanorod heterostructures. *J Phys Chem Lett* 5:590–596
29. Xie H, Hou C, Wang H, Zhang Q, Li Y (2017) S, N co-doped Graphene quantum dot/ TiO_2 composites for efficient photocatalytic hydrogen generation. *Nanoscale Res Lett* 12(1):400
30. Xiang Q, Cheng F, Lang D (2016) Hierarchical layered WS_2 /graphene-modified CdS nanorods for efficient Photocatalytic hydrogen evolution. *Chem Sus Chem* 9:996–1002
31. Lang D, Shen T, Xiang Q (2015) Roles of MoS_2 and graphene as cocatalysts in the enhanced visible-light photocatalytic H_2 production activity of multiarmed CdS nanorods. *ChemCatChem* 7:943–951
32. Wen J, Xie J, Yang Z, Shen R, Li H, Luo X, Chen X, Li X (2017) Fabricating the robust $\text{g-C}_3\text{N}_4$ nanosheets/carbons/NiS multiple heterojunctions for enhanced photocatalytic H_2 generation: an insight into the trifunctional roles of nanocarbons. *ACS Sustain Chem Eng* 5:2224–2236
33. Dong Y, Kong L, Wang G, Jiang P, Zhao N, Zhang H (2017) Photochemical synthesis of Co_3P as cocatalyst for boosting photocatalytic H_2 production via spatial charge separation. *Appl Catal B-Environ* 211:245–251
34. Sun Z, Zheng H, Li J, Du P (2015) Extraordinarily efficient photocatalytic hydrogen evolution in water using semiconductor nanorods integrated with crystalline Ni_3P cocatalysts. *Energy Environ Sci* 8:2668–2676
35. Jin Z, Yang H (2017) Exploration of Zr-metal-organic framework as efficient photocatalyst for hydrogen production. *Nanoscale Res Lett* 12(1):539
36. Yu H, Huang X, Wang P, Yu J (2016) Enhanced photoinduced-stability and photocatalytic activity of CdS by dual amorphous cocatalysts: synergistic effect of Ti(IV) -hole cocatalyst and Ni(II) -electron cocatalyst. *J Phys Chem C* 120:3722–3730
37. Tong X, Kong XT, Zhou Y, Navarro-Pardo F, Selopal GS, Sun S, Govorov AO, Zhao H, Wang Z, Rosei F (2017) Near-infrared, heavy metal-free colloidal “giant” core/shell quantum dots. *Adv Energy Mater*. <https://doi.org/10.1002/aenm.201701432>
38. Tong X, Zhou Y, Jin L, Basu K, Adhikari R, Selopal GS, Tong X, Zhao H, Sun S, Vomiero A, Wang Z, Rosei F (2017) Heavy metal-free, near-infrared colloidal quantum dots for efficient photoelectrochemical hydrogen generation. *Nano Energy* 31:441–449
39. Wang X, Tong R, Wang Y, Tao H, Zhang Z, Wang H (2016) Surface roughening of nickel cobalt phosphide nanowire arrays/Ni foam for enhanced hydrogen evolution activity. *ACS Appl Mater Inter* 8:34270–34279
40. Kresse G, Furthmüller J (1996) Efficient iterative schemes for ab initio total-energy calculations using a plane-wave basis set. *Phys Rev B* 54: 11169–11186
41. Blöchl PE (1994) Projector augmented-wave method. *Phys Rev B* 50: 17953–17979
42. Perdew J, Burke K, Ernzerhof M (1997) Generalized gradient approximation made simple. *Phys Rev Lett* 77:3865–3868
43. Monkhorst HJ, Pack JD (1976) Special points for Brillouin-zone integrations. *Phys Rev B* 13:5188–5192
44. Liang H, Gandi AN, Anjum DH, Wang X, Schwingschlögl U, Alshareef HN (2016) Plasma-assisted synthesis of NiCoP for efficient overall water splitting. *Nano Lett* 16:7718–7725
45. Zhao S, Huang J, Huo Q, Zhou X, Tu W (2016) A non-noble metal $\text{MoS}_2\text{-Cd}_{0.5}\text{Zn}_{0.5}\text{S}$ photocatalyst with efficient activity for high H_2 evolution under visible light irradiation. *J Mater Chem A* 4:193–199
46. Ye L, Han C, Ma Z, Leng Y, Li J, Ji X, Bi D, Xie H, Huang Z (2017) Ni_2P loading on $\text{Cd}_{0.5}\text{Zn}_{0.5}\text{S}$ solid solution for exceptional photocatalytic nitrogen fixation under visible light. *Chem Eng J* 307:311–318
47. Li N, Zhou B, Guo P, Zhou J, Jing D (2013) Fabrication of noble-metal-free $\text{Cd}_{0.5}\text{Zn}_{0.5}\text{S}/\text{NiS}$ hybrid photocatalyst for efficient solar hydrogen evolution. *Int J Hydrogen Energ* 38:11268–11277
48. Yu J, Zhang J, Jaroniec M (2010) Preparation and enhanced visible-light photocatalytic H_2 -production activity of CdS quantum dots-sensitized $\text{Zn}_{1-x}\text{Cd}_x\text{S}$ solid solution. *Green Chem* 12:1611–1614
49. Min Y, Fan J, Xu Q, Zhang S (2014) High visible-photoactivity of spherical $\text{Cd}_{0.5}\text{Zn}_{0.5}\text{S}$ coupled with graphene composite for decolorizing organic dyes. *J Alloy Compd* 609:46–53
50. Feng L, Vrabel H, Bensimon M, Hu X (2014) Easily-prepared dinickel phosphide (Ni_2P) nanoparticles as an efficient and robust electrocatalyst for hydrogen evolution. *Phys Chem Chem Phys* 16:5917–5921
51. Popczun EJ, McKone JR, Read CG, Biacchi AJ, Wilttrout AM, Lewis NS, Schaak RE (2013) Nanostructured nickel phosphide as an electrocatalyst for the hydrogen evolution reaction. *J Am Chem Soc* 135:9267–9270